Universiteit
Leiden
The Netherlands

Anisotropy, multivalency and flexibility-induced effects in colloidal systems

Verweij, R.W.

Citation
Verweij, R. W. (2021, May 27). *Anisotropy, multivalency and flexibility-induced effects in colloidal systems*. *Casimir PhD Series*. Retrieved from https://hdl.handle.net/1887/3179461

Version:	Publisher's Version
License:	Licence agreement concerning inclusion of doctoral thesis in the Institutional Repository of the University of Leiden
Downloaded from:	https://hdl.handle.net/1887/3179461

Note: To cite this publication please use the final published version (if applicable).

Cover Page

Universiteit Leiden

The handle https://hdl.handle.net/1887/3179461 holds various files of this Leiden University dissertation.

Author: Verweij, R.W.
Title: Anisotropy, multivalency and flexibility-induced effects in colloidal systems
Issue Date: 2021-05-27

7 Conformations and diffusion of colloidal rings and dominoes

Ring polymers are special in a topological sense: they do not have a beginning or an end. This results in interesting diffusive and rheological properties. Here, we study model systems of micron-sized flexible rings and dominoes, created from colloid-supported lipid bilayers. We characterize their conformational and diffusive properties. We find that rings and dominoes have a larger translational and rotational diffusion coefficient when compared to chains, while they are less flexible. We show that the flexibility of the rings and dominoes scales as the number of excess floppy modes per bond. Our findings could have implications for the behavior of both synthetic and biological ring polymers, as well as for the dynamic modes of floppy colloidal materials.

7.1 Introduction

Ring polymers have unique properties compared to linear polymers, due to their topologically closed structure that has no beginning or end.[302] Blends of looped and linear polymers can display rich viscoelastic properties[303] that are not only interesting from a physicists' perspective, but can also be used for the design of materials[304] with multifunctional and switchable properties. For example, it was found that tiny fractions of linear polymer chains added to a melt of ring polymers already drastically change their dynamic and rheological properties.[305]

In biological systems, studying the impact of the topological constraints of ring polymers can potentially shed light on how genomes fold themselves into volumes whose linear dimensions are many orders of magnitude smaller than their contour lengths.[306] Interestingly, their diffusivity was found to differ from that of linear polymers: at short timescales, ring polymers exhibit sub-diffusive behavior, long after the stress has completely relaxed, contrary to linear polymers. An explanation of this observation, beyond the fact that shape fluctuations do not necessarily contribute to the overall ring diffusion, requires a detailed understanding of their dynamics.[306,307] However, to measure the dynamics of ring polymers, single-molecule techniques with a simultaneously high spatial and temporal resolution are needed.

Here, we study experimentally and numerically a model system of micron-sized colloidal rings and dominoes, built from spherical colloid-supported lipid bilayers (CSLBs).[85,110,112,242] Colloidal particles may be used as model systems for macromolecules, because of their unique combination of microscopic size and their sensitivity to thermal fluctuations.[18,19,284] Additionally, colloidal particles are useful in their own right, as they could, as an example, provide ways to build switchable materials[285] with novel properties not found in nature. In this work, we consider rings of four to six spherical particles, as well as dominoes of six particles and study both

their conformational and diffusive behavior. Dominoes are clusters of six particles where an additional bond is present compared to rings of the same size, so that the graph of particles and bonds forms a domino, or equivalently, (2, 3)-grid or 3-ladder graph.[308] We find that while the smaller rings and the dominoes show no preferred shapes, preferences arise for the larger rings. Both the translational and rotational diffusivity of the rings and dominoes is greater than that of chains of the same size, while their flexibility is lower. We show that their flexibility scales as the number of excess floppy modes per bond. Our findings could have implications for the behavior of both synthetic and biological ring polymers, as well as for the dynamic modes of floppy colloidal materials.

7.2 Materials and Methods

7.2.1 Experimental

Flexible rings and dominoes of colloid-supported lipid bilayers (CSLBs) were prepared as described in previous work.[85,110,112,242] Specifically, we followed the exact same procedure as in Chapter 5, which we now briefly summarize.

The CSLBs consisting of $(2.12 \pm 0.06)\,\mu$m silica particles were prepared as described in our recent works.[242,244] Briefly, the particles were coated with a fluid lipid bilayer by deposition and rupture of small unilamellar vesicles consisting of 98.8 mol % of the phospholipid DOPC ((Δ9-Cis) 1,2-dioleoyl-sn-glycero-3-phosphocholine), with 1 mol % of the lipopolymer DOPE-PEG(2000) (1,2-dioleoyl-sn-glycero-3-phosphoethanolamine-N-[methoxy(polyethylene glycol)-2000]) and 0.2 mol % of the fluorescently-labeled TopFluor-Cholesterol (3-(dipyrromethene boron difluoride)-24-norcholesterol) or, alternatively, the same amount of the fluorescently-labeled DOPE-Rhodamine (1,2-dioleoyl-sn-glycero-3-phosphoethanolamine-N-(lissaminerhodamine B sulfonyl)). The bilayer coating was performed in a buffer at pH 7.4 containing 50 mM sodium chloride (NaCl) and 10 mM 4-(2-Hydroxyethyl)-1-piperazineethanesulfonic acid (HEPES). We added double-stranded DNA (of respectively strands DS-H-A and DS-H-B, see Table A.1) with an 11 base pair long sticky end and a double stearyl anchor, which inserts itself into the bilayer via hydrophobic interactions, as shown Figure 7.1c. The sticky end of strand DS-H-A is complementary to the sticky end of strand DS-H-B, which allows them to act as linkers. Self-assembly experiments were performed in a different buffer of pH 7.4, containing 200 mM NaCl and 10 mM HEPES. Chains of 2.12 μm CSLBs were formed by self-assembly in a sample holder made of polyacrylamide (PAA) coated cover glass.[244] A confocal microscopy image of the coated particles is shown in Figure 7.1a for a tetramer loop.

7.2.2 Microscopy

Loops and dominoes were imaged for at least 5 min (frame rates between 5 and 19 fps) at room temperature using an inverted confocal microscope (Nikon Eclipse Ti-E) equipped with a Nikon A1R confocal scanhead with galvano and resonant scanning mirrors. A 60× water immersion objective (NA=1.2) was used. 488 and 561 nm lasers

Table 7.1: Overview of the number of measurements, the total duration and the total number of frames per ring size, for the experimental and simulated data, for loops and dominoes.

n	Type	Measurements		Duration [min]		Total frames	
		Exp.	Sim.	Exp.	Sim.	Exp.	Sim.
4	Ring	12	20	92	600	8.5×10^4	2.5×10^7
5	Ring		20		600		2.5×10^7
6	Ring	2	20	11	600	1.2×10^4	2.5×10^7
6	Domino	4	20	75	600	8.5×10^4	2.5×10^7
7	Ring		10		300		1.3×10^7

were used to excite, respectively, the Fluorescein or TopFluor and Rhodamine dyes. Laser emission passed through a quarter wave plate to avoid polarization of the dyes and the emitted light was separated by using 500 – 550 nm and 565 – 625 nm filters.

To complement the data obtained from self-assembled loops and dominoes, we used optical tweezers to assemble specific cluster sizes. For the hexamer loops, the probability of forming such a loop using the self-assembly method we used here is low, therefore these were formed exclusively using optical tweezers. Briefly, we employed a homemade optical setup consisting of a highly focused trapping laser manufactured by Laser QUANTUM (1064 nm wavelength). The laser beam entered the confocal microscope through the fluorescent port, after first passing through a beam expander and a near-infrared shortpass filter. The same objective was used for imaging and to focus the trapping laser beam. During the trapping, the quarter wave plate was removed from the light path.

Particle positions were tracked using a custom algorithm[242] available in TrackPy by using the `locate_brightfield_ring` function[188] or using a least-square fit of a Mie scattering based model implemented in HoloPy.[186] Both methods agree to an accuracy of at least 1 px, however we have found that the Mie scattering based model is more robust for tracking multiple particles in close proximity to each other. For all analysis, we only selected rings and dominoes that showed all bond angles during the measurement time, experienced no drift and were not stuck to the substrate. An overview of the total number of measurements, the total duration and the total number of frames per ring size is shown in Table 7.1.

7.2.3 Simulations

We have performed Brownian dynamics simulations with hydrodynamic interactions following the method outlined in Sprinkle et al.[290] using the open-source RigidMultiblobsWall package.[291] The procedure is identical to the method described in Chapter 6, which we now briefly summarize. Hydrodynamic interactions are calculated using the Stokes equations with no-slip boundary conditions. The hydrodynamic

Table 7.2: **Permutation data.** For the rings and dominoes, we generated the $P(N_\theta, n-2)$ configurations obtained by permuting all possible combinations of opening angles. Interpenetrating configurations, which are forbidden due to excluded volume interactions between particles, were removed from this permutation data. The percentages of clusters of the correct topology are calculated relative to the total number of configurations for permutations of the opening angles between 60 and 300 deg.

n	**Type**	$\delta\theta$ [deg]	$P(N_\theta, n-2)$	**Correct topology [%]**
4	Ring	0.04	3.6×10^7	8.3×10^{-3}
5	Ring	0.5	1.1×10^8	2.4×10^{-2}
6	Ring	2.0	2.0×10^8	5.2×10^{-2}
6	Domino	2.0	2.0×10^8	8.8×10^{-4}

mobility matrix is approximated using the Rotne-Prager-Blake (RPB) tensor,[35] which is a modified form of the Rotne-Prager-Yamakawa (RPY) tensor[34,275,292] and accounts for a bottom wall, which is unbounded in the transverse directions. These corrections to the RPY tensor are combined with the overlap corrections described in Wajnryb et al.[292] to prevent particle-particle and particle-wall overlap. The RPB mobility inaccurately describes near-field hydrodynamic interactions and therefore breaks down for small separation distances. This can be overcome by adding a local pairwise lubrication correction to the RPB resistance matrix as described in detail in Sprinkle et al.[290] Based on the full lubrication-corrected hydrodynamic mobility matrix, the Ito overdamped Langevin equation is solved to describe the effect of thermal fluctuations.

We include a gravitational force on the particles to confine them to diffuse close to the bottom wall, as in the experiments. Inter-particle bonds are modeled by harmonic springs of stiffness $1000 k_B T/R^2$ and equilibrium length $2R$, where $R = 1.06\,\mu$m is the particle radius. The bond angle is not restricted. We set the temperature $T = 298$ K, the viscosity of the fluid $\eta = 8.9 \times 10^{-4}$ Pa s, the gravitational acceleration $g = 9.81\,\mathrm{m\,s^{-2}}$, the particle mass $m_p = 9.5 \times 10^{-15}$ kg (by assuming a particle density of $1900\,\mathrm{kg\,m^{-3}}$) and the simulation timestep $\Delta t = 1.42$ ms. For the firm potential that prevents overlap, we use a strength of $4k_BT$ and a cutoff distance[290,293] $\delta_{\mathrm{cut}} = 10^{-2}$. We initialized the particle loops in the configuration given by the regular polygon of the same size and we used a rectangular configuration, i.e. all opening angles equal to 90 or 180 deg, for the hexamer dominoes. Then, these initial configurations were randomized by running the integration for a simulated time of 60 s prior to saving the configurations, to ensure a proper equilibration of the particle positions, bond lengths, velocities and opening angles. The particle positions were saved every 8 simulation steps to obtain a final framerate of approximately 90 fps. An overview of the total number of simulations, the total duration and the total number of saved frames per cluster type is shown in Table 7.1.

For comparison to the simulated and experimental data, we generated data in which the rings or dominoes are completely non-interacting and freely-jointed up to steric exclusions in the following manner: we generated all $(n-2)$-permutations of the N_θ opening angles θ_i, which gives a total number of $P(N_\theta, n-2) = N_\theta!/(N_\theta - (n-2))!$ combinations of θ_i. Here, the number of opening angles is $N_\theta = (360 - 2 \times 60)/(\delta\theta)$, where $\delta\theta$ denotes the bin width. Then, we removed those combinations that are forbidden because of steric exclusions between particles. After removing these configurations, we checked if the topology of the structure was correct and removed configurations of the wrong topology, resulting in the final allowed combinations, which we call "permutation data". In Table 7.2, we show the bin widths $\delta\theta$ for each n, as well as the total number of generated permutations $P(N_\theta, n-2)$ and the percentage of configurations of the correct topology, i.e. either a ring or a domino.

7.2.4 Diffusion tensor analysis

Definition of the diffusion tensor

We determined the short-time diffusivity of the rings and dominoes, both as function of their instantaneous shape for the tetramer rings, as well as averaged over all possible configurations for all loops and dominoes. Because the rings are sedimented to the bottom substrate, we consider only the quasi-2D, in-plane diffusivity. For the flexible tetramer loops, we calculated a 4×4 diffusion tensor, where the four degrees of freedom correspond to translational diffusivity in x and y, rotational diffusivity and the flexibility of the tetramer loop, which is described by the diffusivity of the opening angle θ. Specifically, the x- and y-directions are schematically shown for one configuration in Figure 7.2a and defined by Equation 7.4. The rotation angle used for determining the rotational diffusivity is indicated in Figure 7.2a and is the angle of the $x(\tau)$ relative to $x(\tau = 0)$, i.e. the angle of the body-centered x-axis of the current frame relative to the body-centered x-axis of the reference frame at $\tau = 0$. The flexibility is calculated from the mean-squared displacement of the opening angle θ, which is depicted in Figure 7.1e. θ is defined in such a way that it is always less than or equal to 120 deg.

The diffusion tensor elements of the tetramer loops were determined analogously to the trimers.[244] Briefly, for each pair of frames, we determined the initial shape of the ring, which is characterized by the opening angle θ. The short time diffusion tensor is then calculated from the trajectories in the following way:

$$\boldsymbol{D}[ij](\theta) \equiv \frac{1}{2} \frac{\partial \langle \Delta i(\theta) \Delta j(\theta) \rangle_\tau}{\partial \tau}, \tag{7.1}$$

with τ the lag time between frames, $\langle \cdots \rangle_\tau$ denotes a time average over all pairs of frames τ apart and $\Delta i(\theta) = i(\theta, t+\tau) - i(\theta, t)$ is the displacement of the i-th diffusion tensor element, which depends on the instantaneous shape given by θ. The average diffusion tensor elements $\boldsymbol{D}[ij]$ were obtained by fitting the overall slope of the mean (squared) displacements as a function of lag time τ. We considered lag times up to

0.25 s, set by the frame rate of the experimental data. We only considered trajectories where the variation in θ did not exceed the edges of the bin describing the initial shape. That is, we divided the possible values of θ in bins and calculated the short-time diffusivity for all combinations of lag times where $\theta(\tau)$ remained in the same bin as $\theta(0)$, which were then stored according to their respective θ-bins. In that way, we calculated the diffusion tensor elements separately for each initial shape.

For fitting the slopes, we used a Bayesian method to find an estimate of the posterior probability distribution, by using an Affine Invariant Markov chain Monte Carlo (MCMC) Ensemble sampler method as implemented in the Python packages `lmfit`[246] and `emcee`.[207] This allowed us to obtain accurate estimates of the error and the maximum likelihood estimate (MLE) of the parameters. Parameter values were initialized using a standard least-square fit, appropriate bounds on the parameter values were implemented as priors. We estimated the autocorrelation time τ_{acor} of the MCMC chain using the built-in methods and ran the analysis for at least $100\tau_{\text{acor}}$ steps, where we discarded the first $2\tau_{\text{acor}}$ steps (corresponding to a burnin phase) and subsequently used every other $\tau_{\text{acor}}/2$ steps (known as thinning). We used 500 independent chains (or walkers). The reported values correspond to the maximum likelihood estimate of the resulting MCMC chains, the reported uncertainties correspond to the 16$^{\text{th}}$ and 84$^{\text{th}}$ percentiles of the obtained posterior probability distribution. For fitting the MSDs, we used a linear model with zero intercept.

For all rings and dominoes, we considered the shape-averaged, quasi-2D translational diffusion coefficient D_T, which corresponds to in-plane diffusivity above the wall. Additionally, we determined the rotational diffusion coefficient $D[\alpha\alpha]$ from the mean squared angular displacement of the x-axis (defined in Equation 7.4, see Figure 7.7a for a schematic depiction for the hexamer loop), which describes the rotational diffusivity around an axis perpendicular to the substrate. Finally, we determine the overall cluster flexibility $D[\boldsymbol{\theta\theta}]$ by calculating the mean squared displacements of the $(n-2)$ opening angles θ_i as follows:

$$\langle|\boldsymbol{\Delta\theta}|^2\rangle = \langle|(\Delta\theta_1, \ldots, \Delta\theta_{n-2})|^2\rangle, \tag{7.2}$$

so that the flexibility $D[\boldsymbol{\theta\theta}]$ is given by

$$\langle|\boldsymbol{\Delta\theta}|^2\rangle = 2(n-2)D[\boldsymbol{\theta\theta}]t, \tag{7.3}$$

analogously to the other diffusion tensor elements.

The definition of the coordinate system

As tracking point, we considered the center of diffusion (c.d.) which coincides with the center of mass of colloidal rings and dominoes, because the choice of origin is expected to affect the magnitude of the diffusion tensor.[105,269] The coordinate system used here is identical to the coordinate system described in Chapter 6 and we briefly summarize its definition here. The c.d. was calculated from $\boldsymbol{A}_{ij}$ defined by Equation 2.16 of Cichocki et al.[269] using the RPB tensor[35] with lubrication corrections as the

inter-particle mobility matrix $\boldsymbol{\mu}_{ij}$. This tensor includes wall corrections, as discussed previously in Section 7.2.3. The c.d. was determined from the simulated particle positions, because the height above the bottom wall was not measured experimentally, but is needed to calculate the wall corrections. The direction of the body-centered x- and y-axes was determined as function of the tracking point $\boldsymbol{r}_{t.p.}$, which defines the origin of the body-centered coordinate frame. We define $\boldsymbol{r}_{t.p.} = \rho_1\boldsymbol{r}_1 + \rho_2\boldsymbol{r}_2 + \cdots + \rho_n\boldsymbol{r}_n$, which defines the location of the tracking point as a linear combination of the particle positions (Equation 2.2 and 2.3 of Cichocki et al.[269]). $\boldsymbol{\rho} = (\rho_1, \rho_2, \ldots, \rho_n)$ is a weight vector which determines how much weight is accorded to each particle in the calculation of the tracking point $\boldsymbol{r}_{t.p.}$. As an example, for a tetramer ring, $\boldsymbol{\rho} = (1/n = 1/4, 1/4, 1/4, 1/4)$ when the tracking point is chosen to be the c.d., or equivalently, the center of mass.

The direction of the x-axis was chosen as

$$\hat{\boldsymbol{x}} = \pm\left[\frac{\boldsymbol{r}_{t.p.,1} + \cdots + \boldsymbol{r}_{t.p.,s_1}}{\rho_1 + \cdots + \rho_{s_1}} - \frac{\boldsymbol{r}_{t.p.,s_2} + \cdots + \boldsymbol{r}_{t.p.,n}}{\rho_{s_2} + \cdots + \rho_n}\right], \tag{7.4}$$

where $\boldsymbol{r}_{t.p.,i}$ is the i-th coordinate of the tracking point and the bead chain is split into two parts with equal numbers of particles according to

$$\begin{cases} s_1 = s_2 = \lceil \frac{n}{2} \rceil & \text{for odd } n \\ s_1 = \lceil \frac{n}{2} \rceil, s_2 = s_1 + 1 & \text{for even } n \end{cases} \tag{7.5}$$

$\hat{\boldsymbol{y}}$ is then chosen such that $\hat{\boldsymbol{x}}$ and $\hat{\boldsymbol{y}}$ form a right-handed coordinate system, where the direction of $\hat{\boldsymbol{y}}$ is chosen to point away from the central part of the cluster towards the tracking point, i.e. along $\boldsymbol{r}_{t.p.} - \left(\boldsymbol{r}_{s_1} + \boldsymbol{r}_{s_2}\right)/2$. This orientation was determined for every frame, which fixed the orientation of the body-centered coordinate system $\boldsymbol{x}(\tau = 0), \boldsymbol{y}(\tau = 0)$. For subsequent lag times, the direction of $\boldsymbol{y}(\tau)$ was chosen such that $\boldsymbol{y}(\tau = 0) \cdot \boldsymbol{y}(\tau) > 0$, i.e. the direction of $\boldsymbol{y}$ does not change sign. The resulting coordinate system relative to the c.d. is visualized for the tetramer loops in Figure 7.2a.

7.3 Results and Discussion

7.3.1 Free energy of flexible tetramer loops

To identify the most likely conformations of micron-sized, flexible ring-like structures in solution, we have studied an experimental model system of colloidal loops and dominoes. Additionally, we have compared our experimental data to Brownian dynamics simulation data, where hydrodynamic interactions between particles and the substrate are taken into account via the Rotne-Prager-Blake (RPB) tensor,[35] overlap corrections[292] and a local pairwise lubrication correction[290] (see Section 7.2.3 for details). The experimental colloidal loops were formed from four or six spherical colloid-supported lipid bilayers (CSLBs).[85,110,112,242] As shown in Figure 7.1c, CSLBs are colloidal silica particles surrounded by a fluid lipid bilayer, which is formed by the rupture and subsequent spreading of small unilamellar vesicles. DNA linkers

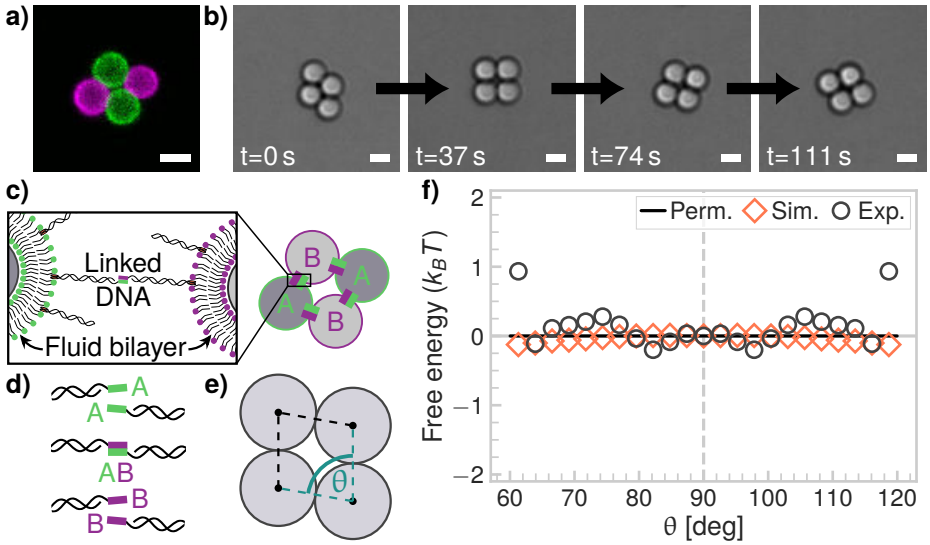

Figure 7.1: **Free energy of flexible tetramer loops. a)** Confocal image and **b)** bright field snapshots of a flexible tetramer ring, which shows shape changes. Scalebars are 2 μm. **c)** The flexible rings are built from colloid-supported lipid bilayers (CSLBs). CSLBs consist of spherical silica colloids coated with a fluid lipid bilayer. DNA linkers are inserted into the bilayer using a hydrophobic anchor. Because the bilayer is fluid, the linkers can diffuse on the surface and therefore, the particles can move with respect to each other whilst staying bonded. **d)** The DNA linkers are functionalized with two complementary sticky ends A and B, so that particles functionalized with A-type linkers can only form bonds with particles coated with B-type linkers. **e)** The definition of the opening angle θ. **f)** The free energy of tetramer rings shows small fluctuations in the ∘ experimental and ⋄ simulated data, but these are insignificant compared to the thermal energy k_BT and absent in the permutation data (Perm.).

with hydrophobic anchors can be inserted into this lipid bilayer. We have used two types of DNA linkers with different single-stranded overhangs, or sticky ends, which we label A and B. As depicted in Figure 7.1d, the A-type sticky end is complementary to the B-type sticky end and therefore, bonds can be formed between the A and B strands only. After such bonds have formed, particles can still rearrange with respect to each other, because the DNA linkers can diffuse in the fluid lipid bilayer. The use of two different sticky ends A and B that are complementary to each other has a distinctive advantage over using a single, self-complementary or palindromic sticky end. Namely, by using two distinct sticky ends, we can prevent adhesion between two opposing A-type or B-type particles in the ring, which would, for a tetramer loop, cause it to lose its reconfigurability. Namely, the tetramer loop would become mechanically rigid because of the extra bond. Moreover, the structure would no longer have a ring topology. In Figure 7.1a, we show a confocal microscopy image

of a tetramer ring. Additionally, in Figure 7.1b we show a time series imaged using brightfield microscopy, in which shape transitions between a diamond and a square configuration of the loop can be observed.

To answer whether there is a preference of either the diamond or square configuration, or even some intermediate configuration, we analyze the free energy of the flexible tetramer loops as function of their opening angle θ, which is schematically depicted in Figure 7.1e. We analyzed the free energy of colloidal rings as function of their shape by calculating the probability density function of the opening angle. From the probability density function calculated from the histogram, we determined the free energy using Boltzmann weighing,

$$\frac{F}{k_B T} = -\ln p + \frac{F_0}{k_B T}, \tag{7.6}$$

where F is the free energy, k_B is the Boltzmann constant, T the temperature, p is the probability density and F_0 is a constant offset to the free energy. As shown in Figure 7.1f, in the simulation data there is a very small preference of $\approx 0.1 k_B T$ for the diamond configuration ($\theta \approx 60$ or 120 deg). On the contrary, in the experimental data, there seems to be a small preference of $\approx 0.3 k_B T$ for $\theta \approx 82$ or 98 deg. Because these preferences are negligible compared to the thermal energy, we conclude that all configurations are essentially equally probable.

7.3.2 Diffusion of flexible tetramer loops

Because all configurations are equally probable, the tetramer loops continuously change their shape. This could have implications for their short-time diffusive behavior, as we have observed previously for colloidal chains[244] (see also Chapter 5 and 6). In Figure 7.2b, we show the shape-dependent, short-time translational diffusivity of the flexible tetramer rings with respect to the coordinate system shown in Figure 7.2a, which is defined in Section 7.2.4. The agreement between the simulated and experimental data is good. In the simulation data, there is virtually no difference between the diffusivity in the x- (Figure 7.2c) and y-direction (Figure 7.2d). Variations in the experimental data are larger, but likely caused by the experimental uncertainty.

The fact that the translational diffusivity does not depend on shape implies that the translational diffusivity of the tetramer rings can be described by the diffusion coefficient of a sphere of some effective radius. Using the lubrication-corrected RPB tensor described in Section 7.2.3, we have calculated the diffusion coefficients of spheres of radii $R_{\text{eq.vol.}}$ and R_g, located just above the substrate. Here $R_{\text{eq.vol.}} = \sqrt[3]{4}R$, i.e. the radius of a sphere with the same volume as the tetramer loop, with $R = 1.06$ μm the radius of an individual sphere of the ring. The radius of gyration R_g is given by

$$R_g = \left[\frac{1}{n^2} \sum_{i=1}^{n} |\boldsymbol{r}_i - \boldsymbol{r}_{c.m.}|^2 \right]^{1/2}, \tag{7.7}$$

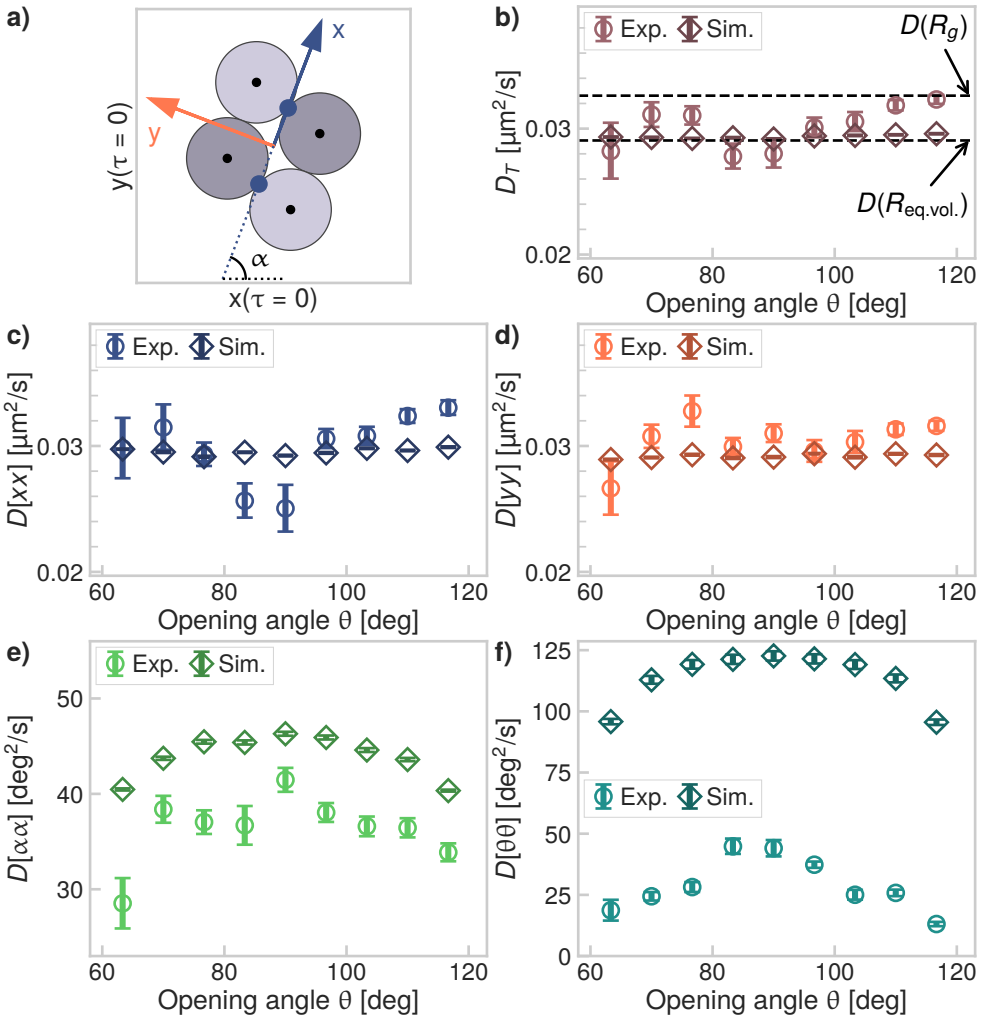

Figure 7.2: **Diffusion of flexible tetramer loops. a)** An illustration of the coordinate system used to analyze the diffusivity of the tetramer rings, as defined in Section 7.2.4. In panels b-f, we have compared the diffusion tensor elements calculated from ⋄ simulated and ∘ experimental data. **b)** The in-plane translational diffusion coefficient D_T. We find that $\langle D_{\text{exp.}}/D_{\text{sim.}} \rangle = 1.03 \pm 0.05$. The translational diffusion along the **c)** x- and **d)** y-directions. **e)** The rotational diffusivity, for which $\langle D_{\text{exp.}}/D_{\text{sim.}} \rangle = 0.83 \pm 0.05$. **f)** Compared to the simulated flexibility, the experimental flexibility is much lower, namely $\langle D_{\text{exp.}}/D_{\text{sim.}} \rangle = 0.25 \pm 0.07$. Both the rotational diffusivity and flexibility terms show a clear maximum for the square configurations, where θ is close to 90 deg. All off-diagonal diffusion tensor elements are close to zero.

where $\boldsymbol{r}_i$ is the position of the i-th sphere and $\boldsymbol{r}_{c.m.}$ is the position of the center of mass of the loop. The resulting near-wall diffusion coefficients are indicated in Figure 7.2b, where we plot the in-plane diffusion coefficient D_T. Comparison of the obtained diffusion coefficients to the experimental and simulated data brings us to the conclusion that the diffusivity of the tetramer rings is captured best by the diffusion coefficient of an effective sphere of the same volume, e.g. a sphere of radius $R_{\text{eq.vol.}}$.

Next, we consider the rotational diffusivity of the loops, which is defined as the in-plane rotation of the x-axis or, equivalently, rotation of the cluster around the out of plane axis, for a plane parallel to the substrate. From Figure 7.2e, we see that the experimentally measured rotational diffusivity is slightly lower than the simulated rotational diffusivity, but both show the same shape dependence. Specifically, the more compact square configuration has a higher rotational diffusivity than the more extended diamond structure, as expected.

Finally, from Figure 7.2f, we conclude that also the flexibility of the tetramer loop depends on its shape: the flexibility is larger for square configurations than for diamond configurations. This indicates that more open structures have a higher flexibility, as we have also observed for chains in Chapter 6. For chains of CSLBs, we have found that the experimental flexibility is 75 to 80 % of the flexibility of the simulated chains, which is probably caused by friction of the DNA linker patch (see Chapter 6). For the tetramer loops, however, we observe a drastically lower flexibility, namely, the experimental flexibility is just 25 % of the simulated one, as shown in Figure 7.2f. This indicates that the tetramer loops experience more interparticle friction compared to the tetramer chains. We will discuss this difference in more detail in Section 7.3.5.

7.3.3 Conformations of pentamer rings

Now that we have characterized the conformations and diffusivity of flexible colloidal tetramer rings, we ask how the possible ring conformations change by increasing the ring size, as this also increases the degrees of freedom of the loop. In order to build a larger ring in our experiments, we need an even number of spheres, because only the A-type DNA linker-coated colloids can bind to the B-type ones, as depicted in Figure 7.1d. This limitation could be overcome in future experiments by using a larger variety of sticky ends, or by using palindromic sequences, where steps should be taken to prevent the formation of more than two bonds per particle. Instead, here we briefly discuss the possible conformations of pentamer loops using only simulated data, before discussing hexamer rings in greater detail.

As shown in Figure 7.3a, the free energy in terms of the opening angles of the pentamer ring shows a preference for angles smaller than 120 deg, for both the simulated and permutation data. This is in contrast with the flat free energy landscape that we have observed for the tetramer rings. The angles are defined in Figure 7.3 and because the angles are indistinguishable, we have used all five opening angles to calculate the free energy.

Next, we have looked at correlations between opening angles θ_i and $\theta_{j>i}$. For the tetramer loop, the two opening angles are perfectly correlated according to θ_2 =

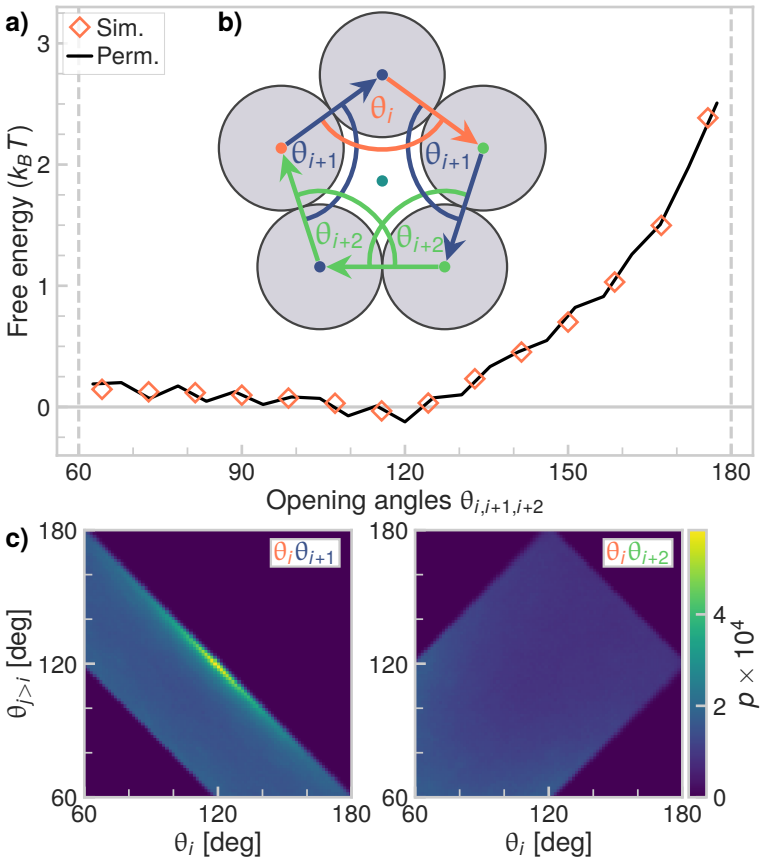

Figure 7.3: **Conformations of pentamer loops. a)** The free energy of pentamer loops as function of one of the opening angles θ_j, with $j \in [i, i+1, i+2]$. The free energy increases as function of θ_j because of constraints imposed by the ring structure. The simulated and permutation data are shown. **b)** Schematic showing the definition of the opening angles θ_j. Three angles are needed to fully describe the conformation of a pentamer ring. **c)** Correlations between the opening angles θ_i and $\theta_{j>i}$ for the simulated data.

180 deg $- \theta_1$. Adding an additional particle to the ring structure also adds a degree of freedom. This can be shown from the Maxwell counting rule, which counts the number of bonds $n_{B,R}$ needed for structural rigidity as[309]

$$n_{B,R} = dn - \frac{d(d+1)}{2} = 2n - 3 \tag{7.8}$$

with $d = 2$ the number of dimensions and n the number of particles. For a loop, there are $n_B = n$ bonds between particles and therefore there are $n_{B,R} - n = n - 3$ degrees of freedom or floppy modes. Going from one floppy mode for the tetramer loop to two for the pentamer loop decreases the correlations between the opening angles, as shown in Figure 7.3c. While the possible combinations of angles $\theta_i\theta_j$ for $j > i$ are still partially constrained by the ring structure, more combinations are geometrically allowed compared to the smaller tetramer rings. We observe that the correlations between any two neighboring opening angles, i.e. θ_i and θ_{i+1}, are stronger than correlations between the more distant opening angles θ_i and θ_{i+2}.

7.3.4 Conformations of hexamer rings and dominoes

We have shown how the free energy of the opening angles of a tetramer loop differs from a pentamer loop, that has an additional floppy mode. The pentamer loop could not be assembled using our experimental scheme. In the experiments, only loops with an even number of particles can be formed, because of the two complementary sticky ends that we use for binding. Therefore, we now study the experimentally accessible extension of the tetramer loop by adding two particles to the ring, so that we obtain hexamer rings. The hexamer rings were formed manually using optical tweezers, because the probability to form them via self-assembly is low. This limitation could be overcome in other ways as well, for example by using template-assisted self-assembly techniques[3] or by using multiple DNA strands to achieve a more fine-grained control over the self-assembly process.[56] In Figure 7.4a, we show a confocal microscopy image of a hexamer ring. From brightfield snapshots in Figure 7.4b, we see that these hexamer rings show a greater variety of shapes compared to the tetramer rings. While the tetramer loop only has one internal degree of freedom, the hexamer loop has three internal degrees of freedom. Its shape can be characterized by four opening angles, depicted in the schematic of Figure 7.4d.

Next, we analyze the free energy of hexamer loops as function of the opening angles in order to determine whether some conformations are preferred over others. Because the loop has no beginning or end, all angles are equivalent and we make a single histogram of the values of all six opening angles. Using Equation 7.6, we obtain the free energy in terms of opening angle, which is shown in Figure 7.4c. For opening angles below $\theta_j \approx 150$ deg, the resulting free energy shows only small variations compared to the thermal energy, for the simulation, permutation and experimental data. For angles larger than $\theta_j \approx 150$ deg, the free energy increases as function of the opening angle and the difference between $\theta_j = 150$ deg and 240 deg is on the order of $4k_BT$. Angles greater than 180 deg correspond to compact and curved structures,

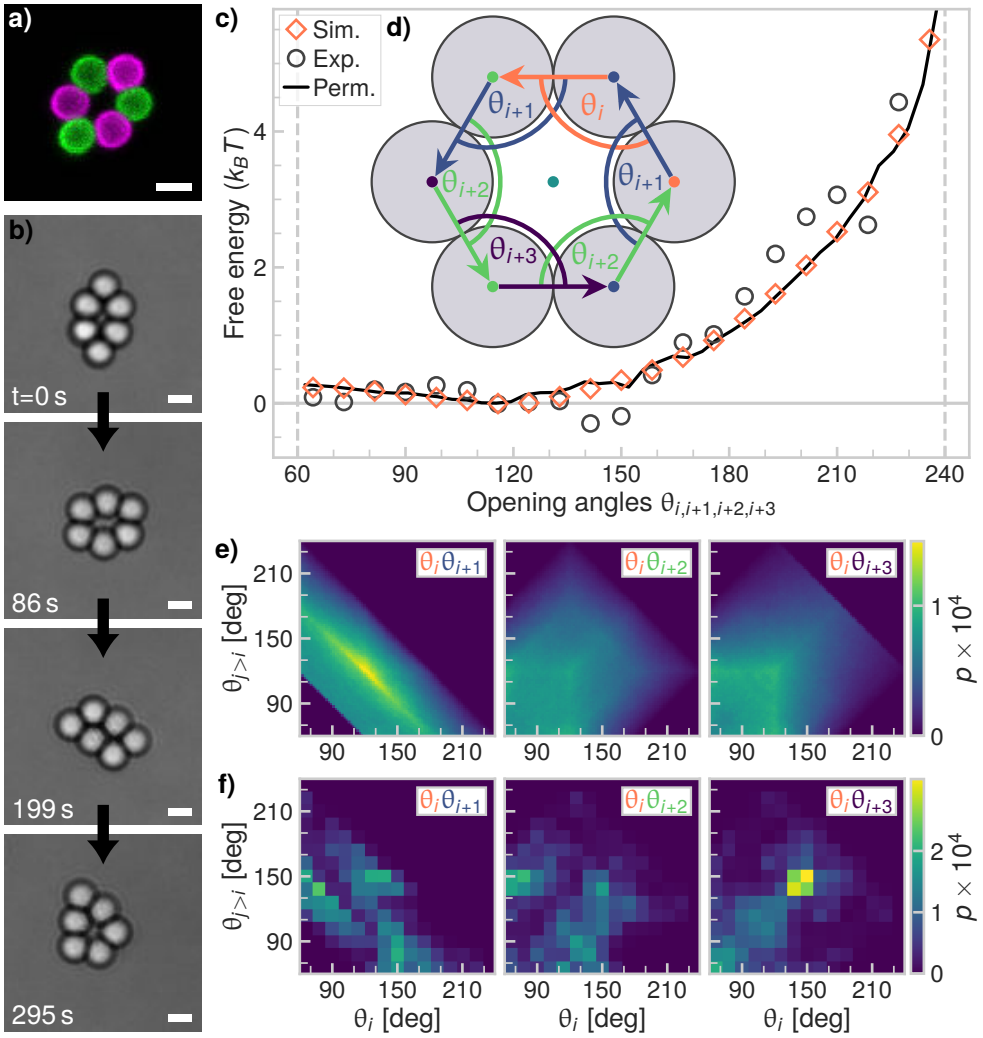

Figure 7.4: **Flexible colloidal hexamer rings. a)** Confocal image. Scalebar is 2 µm. **b)** Snapshots of hexamer rings. A variety of shapes can be observed. Scalebars are 2 µm. **c)** The free energy of hexamer loops as function of the opening angles θ_j, with $j \in [i, i+1, i+2, i+3]$. The free energy increases as function of θ_j because of constraints imposed by the ring structure. The simulated, the permutation and the experimental data are shown. **d)** Schematic showing the definition of the opening angles θ_j. Four angles are needed to fully describe the conformation of a hexamer ring. **e-f)** Correlations between the opening angles θ_i and $\theta_{j>i}$ for **e)** the simulated data and **f)** the experimental data.

which explains why these opening angles are not observed as often as others. For example, there is only one structure in which one of the opening angles is equal to 240 deg.

To study the interplay of the opening angles of the hexamer loops in greater detail, we have calculated the correlations between angles $\theta_i\theta_j$ with $j > i$ for the angles defined in Figure 7.4d, as shown in Figure 7.4e and f for the simulated and experimental data, respectively. For the experimental data, trends are hard to distinguish and more data is needed to disentangle the effect of the four degrees of freedom. Correlations in the simulated data are easier to discern, as shown in Figure 7.4e. The first thing that stands out is that any two neighboring angles are more strongly correlated than more distant opening angles, as can be seen by comparing the correlations between $\theta_i\theta_{i+1}$ to those between $\theta_i\theta_{i+2}$ and $\theta_i\theta_{i+2}$. This is qualitatively the same as what we have observed for pentamer loops. For opening angles θ_i, θ_{i+1} specifically, there is a strong negative correlation given by $\theta_{i+1} \approx 240\,\text{deg} - \theta_i$. Moreover, as expected from the geometry of the ring, it can be seen that the sum of the angles needs to stay within the range $180\,\text{deg} \leq \theta_i + \theta_{i+1} \leq 300\,\text{deg}$. For the correlations between more distant opening angles, the range of accessible angles in Figure 7.4e and f is larger for $\theta_i\theta_{i+2}$ and $\theta_i\theta_{i+3}$ compared to $\theta_i\theta_{i+1}$. Specifically, $\theta_i + \theta_{i+2,i+3} \leq 360\,\text{deg}$ and $\left|\theta_i - \theta_{i+2,i+3}\right| \leq 120\,\text{deg}$. These constraints arise from the topological constraint that the particles form a ring and from the fact that particles cannot interpenetrate each other.

In addition to hexamer rings, hexamer dominoes can also be formed via self-assembly. In fact, their formation is more likely than that of hexamer rings, because they can be obtained from a greater number of initial cluster topologies, such as tetramer loops and related structures. The structure we call a hexamer domino is a (2, 3)-grid, 3-ladder or domino graph[308] where the particles are situated on the vertices, as shown in the confocal image of Figure 7.5a and in the brightfield snapshots of Figure 7.5d. As depicted by the schematic in Figure 7.5b, the hexamer domino has the same structure as the hexamer ring of Figure 7.4, but one extra bond, as indicated by the yellow circle.

Because of the extra bond, the hexamer dominoes behave very differently compared to the hexamer rings. While the rings have three floppy modes, the dominoes have only two, as given by Equation 7.8. Their possible variety in shapes is therefore smaller, as shown in Figure 7.5d. In turn, their conformations can be uniquely described by two opening angles instead of four angles for the hexamer loop, as shown in the schematic in Figure 7.5c, where we also define the indices of all six opening angles. Taking the same approach as for the hexamer rings, we have calculated the free energy as function of the opening angles. However, because for the dominoes not all opening angles are indistinguishable from each other, we consider the opening angles $\theta_{\alpha,i}$ and $\theta_{\beta,j}$ separately, as shown in Figure 7.5e for the experimental, simulated and permutation data. The resulting free energy landscape is markedly different from the one for hexamer rings in Figure 7.4c because of the additional bond that is formed. For $\theta_{\alpha,i}$, the free energy landscape is very similar to that of the tetramer loops in

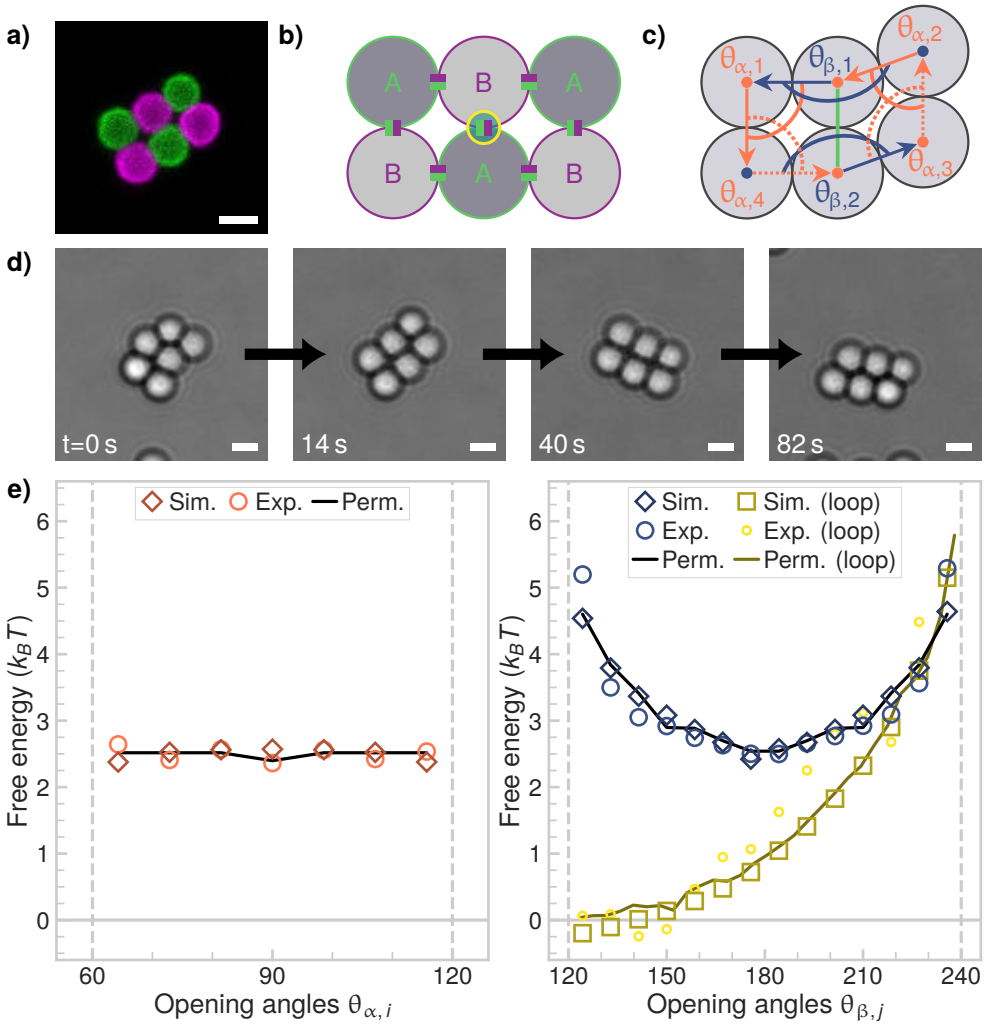

Figure 7.5: **Flexible hexamer dominoes. a)** Confocal image of a hexamer domino cluster. Scalebar is 2 µm. **b)** An additional bond is formed for the hexamer dominoes compared to the loops shown in Figure 7.4, as indicated by the yellow circle. **c)** Schematic of the definition of the opening angles. Only two angles are needed to fully describe the conformations of the dominoes. **d)** Brightfield microscopy images of hexamer dominoes. Due to the additional bond compared to the rings in Figure 7.4, a smaller variety of shapes is possible. Scalebars are 2 µm. **e)** The free energy of hexamer dominoes as function of the opening angles $\theta_{\alpha,i}$ (left) and $\theta_{\beta,j}$ (right), as defined in panel c. The simulated, the permutation and the experimental data are shown.

Figure 7.1f. This makes sense because the hexamer domino essentially consists of two flexible tetramer loops that share one side. The angles $\theta_{\beta,j}$ are the opening angles between the two tetramer loop segments, as indicated in the schematic in Figure 7.5c. For those angles, the most likely value lies around 180 deg. We show the free energy of the hexamer rings in the same panel of Figure 7.5e. It is clear that the free energy of the dominoes for $\theta_{\beta,j}$ partially overlaps with the free energy of the hexamer rings for $\theta_{\beta,j} > 210$ deg, because both correspond to compactly curved shapes. For the dominoes, the free energy is symmetric around 180 deg as curving the structure as shown in Figure 7.5c "upwards" (e.g. $\theta_{\beta,1} > 180$ deg) or conversely, "downwards" (e.g. $\theta_{\beta,1} < 180$ deg) results in the same shape.

In conclusion, in this section we have characterized the possible conformations of flexibly-linked colloidal hexamer rings and dominoes. Contrary to the tetramer loops, we have found that there are preferred values of the opening angles for the hexamer loops and dominoes. These have, compared to tetramer loops, one and two additional degrees of freedom for dominoes and rings, respectively. Our results show that the exact topology of a flexible structure and especially the number of floppy modes, have a large effect on whether or not certain conformations are preferred over others.

7.3.5 Gyration radii of rings, dominoes and chains

So far, we have characterized the behavior of flexibly linked tetramer, pentamer and hexamer loops, in addition to flexible hexamer dominoes. Now, we compare their conformational and diffusive behavior to each other and to flexibly linked chains of the same number of spheres. A natural measure to compare the tetramer and hexamer rings is the radius of gyration R_g as defined in Equation 7.7, which is a measure for the size of the loops. Furthermore, it is often used to quantify the extent of polymer chains, or, as we have discussed in Chapter 6, for flexibly-linked colloidal bead-chains.

The theoretical radius of gyration of tetramer loops is constant and its value is equal to $b/\sqrt{2} \approx 0.708b$, with b the bond length. From the experimental and simulated data, we obtain R_g values of $(0.71 \pm 0.01)b$ and $(0.708 \pm 0.004)b$, respectively. This slight spread around the expected value of R_g can be attributed to variations in the bond length b. These variations are most likely caused by tracking uncertainties and the limited wiggle room stemming from the DNA linkers in the experimental data. In the simulated data, these variations stem from the variations in particle separation distance allowed by the harmonic potential that keeps the particles bonded. Altogether, deviations from the expected radius of gyration are small. Tetramer chains on the other hand, show a variation in R_g from $0.71b$ to $1.12b$ with a median value of $0.93b$ (see Chapter 6). That is, their minimal size measured by R_g is equal to the size of a loop, which is the most compact structure of four particles, but on average the chains are more extended. This has implications for the diffusivity as well, which we will discuss in Section 7.3.6.

Contrary to tetramer loops, the radius of gyration of pentamer rings is not constant.

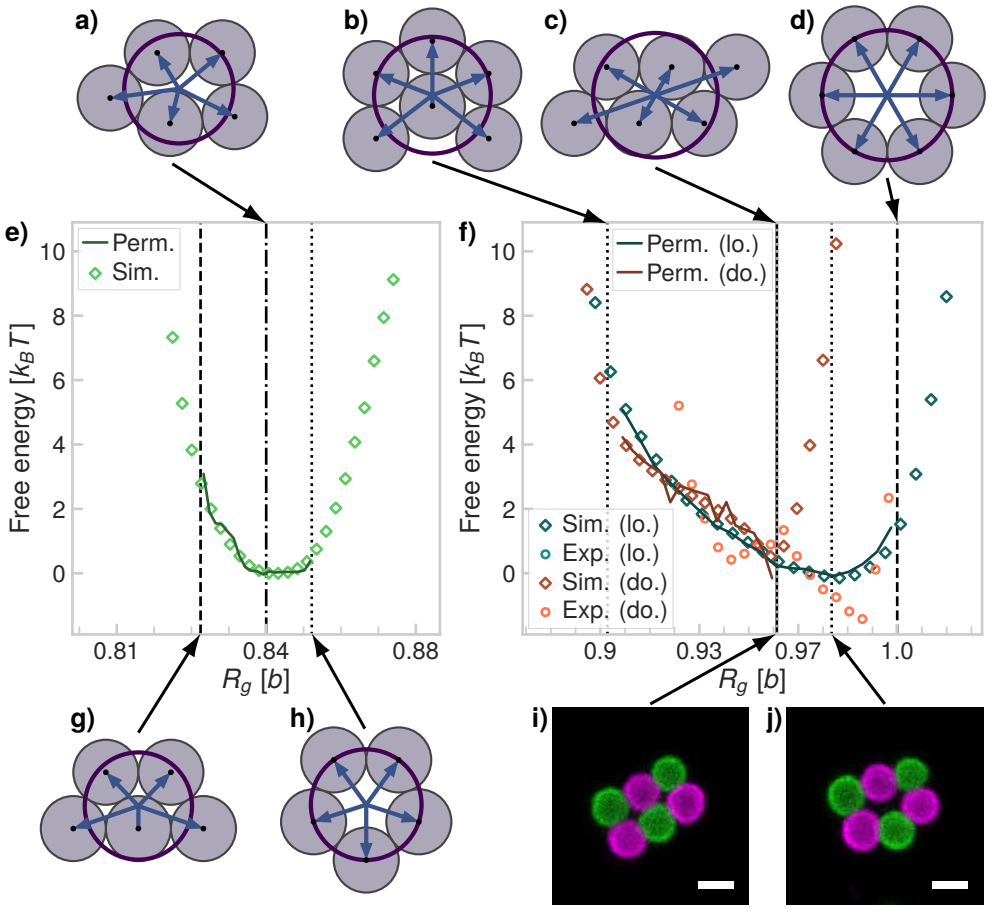

Figure 7.6: **Radius of gyration of pentamer and hexamer rings and dominoes.** Schematics of **a)** a pentamer ring, **b)** the most compact hexamer ring, **c)** a hexamer ring or domino, **d)** the regular hexagon, which is the most extended hexamer ring. **e-f)** The free energy as function of the radius of gyration normalized by the average bond length b for **e)** pentamer and **f)** hexamer loops (lo.) and dominoes (do.). Experimental, simulated and permutation (Perm.) data are shown. The R_g values corresponding to the schematics are indicated on the plot, as well as the R_g values corresponding to the structures shown in the confocal images of panels i and j. **g-h)** Schematics of **g)** the most compact and **h)** the most extended pentamer loop. **i-j)** Confocal images of **i)** a hexamer domino and **j)** a hexamer ring. Scale bar are 2 µm. In panels a-d and g-h, a circle centered at the c.m. with a radius equal to the radius of gyration is shown for all structures.

In Figure 7.6e, the free energy of pentamer rings is shown in terms of R_g. There is a preference for structures of R_g value between the conformation shown in the schematic of Figure 7.6a and the most extended structure with the largest R_g, which is the regular pentagon schematically shown in Figure 7.6h. The free energy of the most compact conformation, which is depicted in Figure 7.6g, is approximately $3k_BT$ higher than that of the more extended structures. We note that the range of R_g in the simulated data exceeds that of the permutation data, which again is caused by variations in the bond length b. However, these variations are smaller than 5 % of the average R_g. Again, the radius of gyration of the rings is much smaller than that of the pentamer chains in Chapter 6, which varies between the smallest value observed for the ring structure in Figure 7.6g and approximately $4b$. This will affect their diffusivity as well, as we will discuss in Section 7.3.6.

Following the same trend, the hexamer rings show larger variations in R_g compared to the pentamer rings. The distribution between the most compact shape depicted in Figure 7.6b and the most extended shape in Figure 7.6d is not symmetric: we find a minimum in the free energy in terms of R_g for structures that correspond to the confocal microscopy image shown in Figure 7.6j, as can be seen from the free energy plotted in Figure 7.6f. In the same graph, we show the free energy of hexamer dominoes in terms of R_g. We find that the possible variation in R_g is smaller for the dominoes compared to the rings, as is expected because they have one degree of freedom less than the rings and as a result, can adopt a smaller variety of conformations. Additionally, the dominoes are on average more compact than the rings, but show the same trend in free energy as function of R_g. This difference indicates that the average diffusivity of hexamer dominoes will also differ from hexamer rings, as we will discuss in Section 7.3.6, where we will also compare their diffusivity to hexamer chains. Finally, we stress that R_g does not uniquely define the shape of the rings and dominoes, as can be seen by comparing the schematic of Figure 7.6c to the confocal image of Figure 7.6i, which have a different conformation but the same value of R_g. Nonetheless, we have shown that the radius of gyration is a useful measure to compare the free energy of a variety of different structures of different topologies in terms of their extent, which in turn affects their diffusive properties.

7.3.6 Shape-averaged diffusivity of rings, dominoes and chains

Having shown that the radius of gyration of the rings and dominoes is smaller on average than that of chains, we now compare the average diffusivities of rings, dominoes and chains. To do so, we analyze the diffusivity of the relative to the same definition of the coordinate system for all structures as defined by Equation 7.4 and depicted schematically in Figure 7.2a for the tetramer loops, in Figure 7.7a for the hexamer rings and in Chapter 6 for the chains.

First, we compare the average translational diffusivity of all structures in Figure 7.7b. The translational diffusivity of rings decreases as function of their size, as expected and as we have previously shown for flexible chains. In the experiments, however, both diffusivities are the same, and we conclude that more data is needed to reliably

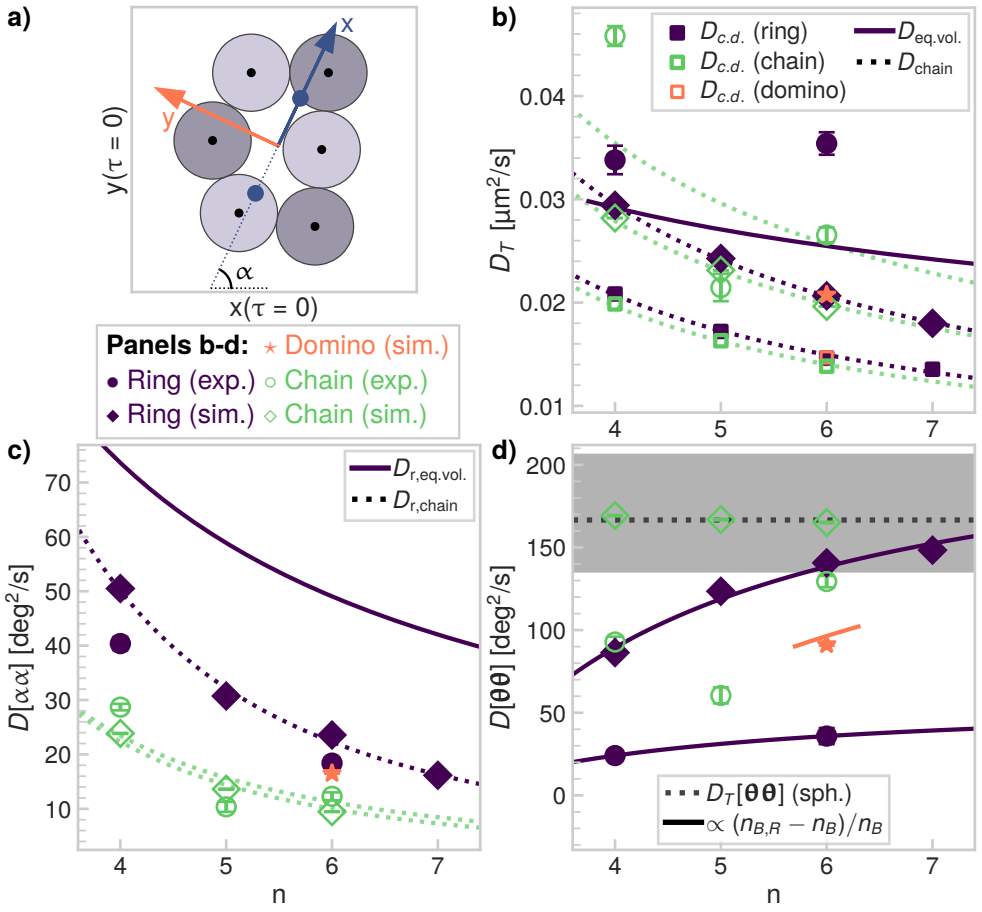

Figure 7.7: **Shape-averaged diffusivity of rings, dominoes and chains. a)** A schematic depiction of the coordinate system used to analyze the diffusivity of hexamer rings, as defined in Section 7.2.4. For all structures, the same equations are used to determine their coordinate system. The symbols and colors that correspond to the different structures are indicated in the legend. **b)** Translational diffusivity of rings, dominoes and chains. **c)** Rotational diffusivity of rings, dominoes and chains. **d)** The flexibility of rings, dominoes and chains, compared to the expected flexibility $D_T[\boldsymbol{\theta\theta}]$, as calculated from the translational diffusivity of a single sphere. We find that the flexibility of rings and dominoes shows the same scaling as function of n, as given by Equation 7.11.

determine the diffusivity of the hexamer rings. Nevertheless, for the tetramer rings, the experimental diffusivity is slightly larger than in the simulations, as we had observed previously for the flexible chains in Chapter 6. We hypothesize this is due to the no-slip boundary condition on the substrate that is used in the simulations, while in the experiments the substrate is a hydrogel that has a finite slip length, as we have argued in Chapter 6. We find that the hexamer dominoes have the same translational diffusion coefficient as the hexamer rings. This is unexpected, because by comparing their average radii of gyration, we have found that $\langle R_g \rangle$ of the dominoes is smaller than that of the rings, as shown in Figure 7.6. However, the differences between the two are very small, which may explain why their diffusion coefficients are very similar.

Compared to chains of the same size, the translational diffusivity of the rings in the simulation data is slightly larger, as is expected based on our analysis in Figure 7.6, where we have found that the average radius of gyration of the rings is smaller than that of the chains (characterized in Chapter 6). This can also be seen from the lower bound on the diffusivity $D_{c.d.}$ as calculated from the matrix $\boldsymbol{A}_{ij}$ defined by Equation 2.16 of Cichocki et al.[269] using the RPB tensor[35] with lubrication corrections as the inter-particle mobility matrix $\boldsymbol{\mu}_{ij}$, as explained in Section 7.2.4. For the experimental data, the trends are less clear and more data is needed to fully elucidate their behavior.

The rotational diffusivity of the rings, dominoes and the chains are shown in Figure 7.7c. There, we see that both the experimental and simulated rotational diffusivity of the rings is larger than that of the chains, because of their smaller average radius of gyration. For the same reason, the rotational diffusivity of the rings decreases as function of their size and the rotational diffusivity of the dominoes is smaller than that of the rings. We hypothesize that the reason why we measure a lower rotational diffusivity for the dominoes compared to the rings and not a lower translational diffusivity can be explained as follows. Based on the Stokes relations, the rotational diffusivity scales as $1/R^3$, while the translational diffusivity scales as $1/R$. Therefore, small differences in the average radius have a larger effect on the rotational diffusion coefficient than on the translational one, which may explain why the differences between the dominoes and rings are only appreciable for the rotational terms.

Having discussed the relative magnitudes of the translational and rotational diffusivity of all structures, we now consider the scaling of these terms for the rings as function of their size. There are different scalings that could reasonably be expected. First, for tetramer rings in Figure 7.2b, we have found that the shape-dependent short-time diffusivity can be accurately described by the diffusion coefficient of a sphere of the same volume as the ring, which we label as $D_{\text{eq.vol.}}$ in Figure 7.7b. Here, we used the lubrication-corrected RPB tensor described in Section 7.2.3 to calculate the diffusion coefficients of spheres of radii $R_{\text{eq.vol.}} = \sqrt[3]{n}R$, located just above the substrate. While it is clear from Figure 7.7b that $D_{\text{eq.vol.}}$ is close to the diffusion coefficient of the flexible tetramer rings, for larger ring sizes $D_{\text{eq.vol.}}$ deviates greatly from the diffusion coefficients obtained from the simulated data. Moreover, the rotational diffusion coefficients $D_{\text{r,eq.vol.}}$ predicted from spheres of the same volume as

the rings overestimates the rotational diffusivity as found from the simulated data, as shown in Figure 7.7c. Additionally, we have compared our data to the translational and rotational diffusion coefficients of a spheroid, calculated using the Perrin friction factors.[31,310] For this comparison, we have used the lengths of the long and small axes of the spheroid, as well as a prefactor that models additional substrate friction as fitting parameters. Similarly to the diffusion coefficients calculated from a sphere of the same volume, we observed large deviations between the spheroid model and the simulated diffusion coefficients (not shown).

Instead, we find that both the translational and rotational diffusivity of the rings can be accurately modeled by the scalings we had previously found for flexible chains in Chapter 6, namely

$$D_{chain} \propto \left(a b_K \left[(n^2 - 1)/n \right]^{\nu} \right)^{-\nu/2} \tag{7.9}$$

$$D_{r,chain} \propto \frac{\ln\left(2L/b_K\right)}{L^3}, \tag{7.10}$$

where we use the values we have determined in Chapter 6. Namely, the constant $a = 0.349 \pm 0.002$, $b_K = (1.03 \pm 0.01)b$ is the Kuhn length (approximately equal to the average bond length), ν is the Flory factor (expected to be 3/4 for chains in 2D) and we set $L = b_K(1 + (n-1)^{\nu})$. Briefly, D_{chain} and $D_{r,chain}$ are derived from Kirkwood-Riseman theory for the diffusivity of polymers using the rigid body approximation,[286] as explained in detail in Chapter 6. We have only fitted the simulated data using these expressions, in order to obtain the scaling from the experimental data, more measurements are necessary. From the fit of the translational diffusivity of the rings we obtain $\nu = 0.81 \pm 0.01$ and from the fit of the rotational diffusivity we find $\nu = 0.83 \pm 0.04$. These are close to each other and moreover, close to the values obtained in Chapter 6 for chains, where we have found $\nu = 0.77 \pm 0.02$ for the translational and $\nu = 0.83 \pm 0.04$ for the rotational diffusivity of flexible chains. This good agreement between the proposed scaling and the simulated and experimental data shows that the rings behave on average more as rod-like objects than as sphere-like objects, in terms of their diffusivity.

Finally, we consider the shape-averaged flexibility in Figure 7.7d as defined by Equation 7.3. The experimentally measured flexibility of the rings is much lower than the simulated flexibility, namely, the experimental value is (27 ± 1) % of the simulated value on average. For the flexible chains, we have found that the experimental flexibility is 75 to 80 % of the simulated flexibility, which we attribute to friction of the DNA linker patch not modeled in the simulations, as discussed in Chapter 6. This is also true for the rings, but because the difference in experimental and simulated flexibility is much larger for the rings, there could be an additional source of friction present for the rings that is not modeled in the simulation data. Alternatively, while for the chains, the number of average bonds per particle is always less than one ($n_B/n = (n-1)/n$), for the rings, the average number of bonds per particle is

always equal to one ($n_B/n = n/n$). Therefore, the average friction per particle, stemming from the DNA linker patch, might be larger for the individual spheres in a ring compared to those in a chain of the same length. Additionally, because the friction depends on the DNA linker concentration in the patch area,[85] it could be that by performing more experiments using different DNA linker concentrations, we recover the same behavior as we previously observed for chains in Chapter 6.

Counter-intuitively, we find that for both the simulated and experimental data, the flexibility of the rings increases as function of ring size. This is unexpected because, for the chains, we have found that the flexibility is set by the translational diffusivity of the individual spheres, as indicated in Figure 7.7d by $D_T[\boldsymbol{\theta\theta}]$ and discussed in Chapter 6. For the rings however, the flexibility is lower than this value, both in the simulated and experimental data. Therefore, we hypothesize that both the smaller separation distances between particles in the rings, as well as the additional topological constraint of the ring structure, leads to a lower flexibility compared to the more extended chains. Indeed, as shown in Figure 7.7d, we find that the simulated data of the rings can be described by the following scaling based on Equation 7.8

$$D[\boldsymbol{\theta\theta}] = D_{\boldsymbol{\theta\theta},0} + \Delta D_{\boldsymbol{\theta\theta}} \frac{n_{B,R} - n_B}{n_B} = D_{\boldsymbol{\theta\theta},0} + \Delta D_{\boldsymbol{\theta\theta}} \frac{n-3}{n}, \tag{7.11}$$

where $D_{\boldsymbol{\theta\theta},0}$ and $\Delta D_{\boldsymbol{\theta\theta}}$ are fit parameters, n_B is the number of bonds and $n_{B,R}$ is the number of bonds required for structural rigidity as given by Equation 7.8. The good agreement between the simulated data and Equation 7.11 implies that the flexibility of the rings scales as the number of excess floppy modes given by $n_{B,R} - n_B$, as obtained from the Maxwell counting rule given in Equation 7.8, divided by the total number of bonds n_B. By fitting the simulated data of the flexible rings, we find $D_{\boldsymbol{\theta\theta},0} = (40 \pm 9)\,\mathrm{deg}^2/\mathrm{s}$ and $\Delta D_{\boldsymbol{\theta\theta}} = (196 \pm 21)\,\mathrm{deg}^2/\mathrm{s}$. Now that we know this scaling is valid for the simulated data, we can fit the same relation to the experimental data, for which we find that $D_{\boldsymbol{\theta\theta},0} \approx 12\,\mathrm{deg}^2/\mathrm{s}$ and $\Delta D_{\boldsymbol{\theta\theta}} \approx 47\,\mathrm{deg}^2/\mathrm{s}$. We find that values of the fit parameters determined from the experimental data are respectively 29 and 24 % of the fit parameters determined from the simulated data, which is also close to the average ratio between the experimental data and simulated data, which is (27 ± 1) %. Therefore, we conclude that the experimental data follows the same scaling.

Interestingly, we can further test whether the proposed scaling is valid by comparing the flexibility of the hexamer dominoes to the flexibility predicted by Equation 7.11. According to the proposed scaling, the relation between $D[\boldsymbol{\theta\theta}]$ and n should be different for rings and dominoes, because of the different number of bonds. For the rings, we have found that $D[\boldsymbol{\theta\theta}] \propto (n-3)/n$, while for the dominoes $D[\boldsymbol{\theta\theta}] \propto (n-4)/(n+1)$ if Equation 7.11 holds. In Figure 7.7d, we plot the expected scaling for the hexamer dominoes using the fit values obtained from the simulated data of the rings. We find that indeed, the simulated flexibility of the hexamer dominoes is close to the predicted value based on Equation 7.11. While more work is required to conclusively show that the scaling we have found is indeed valid

for both rings and dominoes, we have presented strong indications that this is the case. This finding could also have implications for the expected flexibility of floppy colloidal crystal structures, for which we expect the flexibility will be lower than $D_T[\boldsymbol{\theta\theta}]$ as well, according to the scaling we have found here.

7.4 Conclusions

In this chapter, we have studied the possible conformations and the diffusive behavior of flexibly-linked colloidal rings. We have found that the tetramer loops show no preference for any configuration and freely change their shape from square- to diamond-like conformations. Their short-time diffusivity only weakly depends on shape and their translational diffusion can be described by the diffusion coefficient of a sphere of the same volume.

In addition to tetramer rings, we have studied the possible conformations of larger rings. The added degrees of freedom lead to preferred configurations for rings larger than the tetramer ring. Furthermore, we have compared hexamer rings to hexamer dominoes, that have an additional bond compared to the rings. For the dominoes, the preferred conformations lie between those of the hexamer loops and the tetramer loops because of the unique topology of the dominoes, which can be thought of as consisting of two coupled tetramer loops.

Finally, we have compared the shape-averaged diffusivity of rings, dominoes and chains. The shape-averaged short time diffusivity of rings decreases as function of their size and the rings diffuse slightly faster than chains of the same number of spheres, because the rings have a smaller average radius of gyration. The same trends can be observed for the rotational diffusivity. Both scale according to the scaling we have found for flexible chains in Chapter 6, where we have modeled the clusters as instantaneously rigid by following the Kirkwood-Riseman theory.[286]

The flexibility of rings, however, is smaller compared to the flexibility of the chains. We have found strong indications that the flexibility of the rings and dominoes scale as the number of excess floppy modes of the structure divided by the total number of bonds. This finding could have implications for the assembly of floppy colloidal crystal structures, for which we expect the flexibility will be severely hindered as well. As an example, the scaling we have found predicts that for a square $n \times n$ floppy colloidal crystal, the flexibility will scale as $(2n-3)/(2n^2-2n)$ which is a decreasing function for $n \geq 2$ and approaches zero in the limit of infinitely large n. For future work, it would be interesting to test whether the proposed scaling is valid for these square floppy lattices as well and if so, up to what lattice size. More broadly, our findings could have implications for the diffusive behavior of both synthetic and biological ring polymers.

Acknowledgments

We thank Loes Huijnen and Indrani Chakraborty for additional experimental data. We thank Ali Azadbakht for the design and setup of the Optical Tweezers and his technical support. We are grateful to Aleksandar Donev and Brennan Sprinkle for

fruitful discussions and for providing us with example code for the simulations. The simulations were partly performed using the ALICE compute resources provided by Leiden University. This project has received funding from the European Research Council (ERC) under the European Union's Horizon 2020 research and innovation program (grant agreement no. 758383).